Supplemental Materials

1. Methods

1.1. Power spectral density estimation

Power spectral density (PSD) was measured for 600 ms blocks gathered from the interstimulus baseline signal. (The μECoG signal was resampled at 4 kHz after a Chebychev Type-I lowpass filter with a corner frequency 1.6 kHz and 20 dB attenuation at 2 kHz.) Thomson's multitaper method was used with a time-bandwidth product of 3.5 (giving an estimator resolution of 11.7 Hz), and blockwise PSDs from all channels were averaged for each recording session.

1.2. Bayesian semivariance modeling

We used the spatial semivariance function to describe dissimilarity of recorded signals as a function of the straight-line distance between sites $\gamma(h_{ij}) = \frac{1}{2}\mathrm{var}\{x_t(s_i) - x_t(s_j)\}$ ($h = \| s_i - s_j \|$). Under the assumption of second order stationarity, the semivariance function can be posed in terms of the spatial autocovariance function, which can be further split into uncorrelated process and noise components.

$$\begin{aligned}\gamma(h) &= C_x(0) - C_x(h) \\ &= \underbrace{\sigma_n\big(1 - \delta(h)\big)}_{noise} + \underbrace{C_{LFP}(0) - C_{LFP}(h)}_{process}\end{aligned}$$

While the semivariance must be zero at a distance of zero, the noise component introduces an abrupt step in mean square difference at $h > 0$. Absent this discontinuity, the semivariance of the neural potential field is assumed to be smooth and monotonic, and was modeled by the Matérn covariance function. To reduce complexity of the model, we fixed the smoothness parameter of the Matérn function at $\nu = 3/2$, which showed good agreement with the close-range covariance of our electrode recordings. The constrained covariance function was parameterized only by a length-scale θ, at which distance the normalized correlation falls to about 0.5

$$C(h;\theta) = (1 + \frac{\sqrt{3}h}{\theta})\exp\{\frac{-\sqrt{3}h}{\theta}\}$$

We estimated the amplitude, length-scale, and noise floor of the μECoG potential field's spatial semivariance using hierarchical Bayesian modeling. The amplitude (upper asymptote) of the field semivariance was given a Normally distributed prior with mean *s* and variance t^2 estimated from the top quartile of empirical semivariance samples. The noise level (re-parameterized for convenience) was taken as a proportion of this scale, with a Beta prior having approximately 90% mass below 0.5.

$$\zeta \sim \mathcal{N}(s, t^2)$$

$$\rho_n \sim Beta\left(\frac{1}{2}, 2\right)$$

$$\sigma_n = \rho_n \zeta$$

With a flat prior over the length-scale θ, the probabilistic model of the observed semivariance pairs was modeled as multivariate Normal with the following form

$$L(h) = (\zeta - \sigma_n)\big(1 - C(h;\theta)\big) + \sigma_n$$

$$\gamma(h) \sim \mathcal{N}(L(h), \varepsilon^2 I)$$

We used Monte Carlo Markov Chain (MCMC) (implemented in PyMC3 [82]) to sample the joint posterior of $\{\zeta, \rho_n, \theta, \varepsilon^2\}$ given the empirical semivariance pairs, and reconstruct posterior predictive samples of the model semivariance curve. A "Bayesian" goodness of fit coefficient was computed by comparing the median posterior value of residual variance ϵ^2 from the hierarchical model with the sample variance of the empirical semivariance. For semivariance γ_n computed from *N* electrode pairs,

$$\mathrm{R2}_B = 1 - \frac{N\mathrm{med}\{\varepsilon^2\}}{\sum_n (\gamma_n - \bar{\gamma})^2}$$

2. Results

2.1. Device failure following accelerated aging

Devices fabricated with LCP encapsulation demonstrated more consistent performance across multiple manufacturing batches compared to PI arrays (supplemental figure 2).

Energy dispersive spectroscopy of Sample C from LCP (Batch 1) confirmed that the corrosion of the gold-plated sterling silver reference led to silver and copper deposits on the μECoG contacts after 368 days of accelerated aging (supplemental figure 3).

2.1. Baseline signal statistics

Longitudinal PSDs (supplemental figure 4) showed that signal power declined over the duration of implants in similar proportions for all bands, including the 10-100 Hz band depicted in figure 4 of the main text.

Spatial field semivariance models fit the distribution of observed semivariance with an average R2 of 0.414 ± 0.192 (mean ± SD, supplemental figure 5). We tested trends in time and in relation to the median posterior estimate of signal amplitude ζ using LMMs with random effects per implant. Although variable, goodness of fit neither increased nor decreased over the duration of implants, with no significant slope over time ($X_1^2 = 0.029$, p=0.864, likelihood ratio test). Further, $R2_B$ was not affected by changing signal amplitude ($X_1^2 = 0.172$, p=0.679, likelihood ratio test).

2.2. Evoked response SNR

Longitudinal evoked responses and ESNR maps are given for all implants in supplemental figure 6. In most highlighted channels, the arrays recorded evoked waveforms with consistent features across the duration of the implantation. The depiction of trial-averaged responses obscures the true variability of response and baseline μECoG, which are more accurately described with the random vector distance summarized in ESNR.

2.3. Tone decoding

Tone frequencies were predicted from μECoG timeseries of the auditory evoked response, and decoding was summarized by accuracy (rate of successful prediction) and error (average magnitude of mistakes) in octaves. Accuracy responses were interpreted as binomial variates, while the linear mean-variance scaling of the error responses suggested a negative binomial generalized linear model (supplemental figure 7(a-b)). Accuracy and error per recording session were regressed onto median array impedance with random effects per implant, resulting in little chronic-phase dependence on impedance and hence stable decoding results (supplemental figure 7(c-f)).

Supplemental Figures

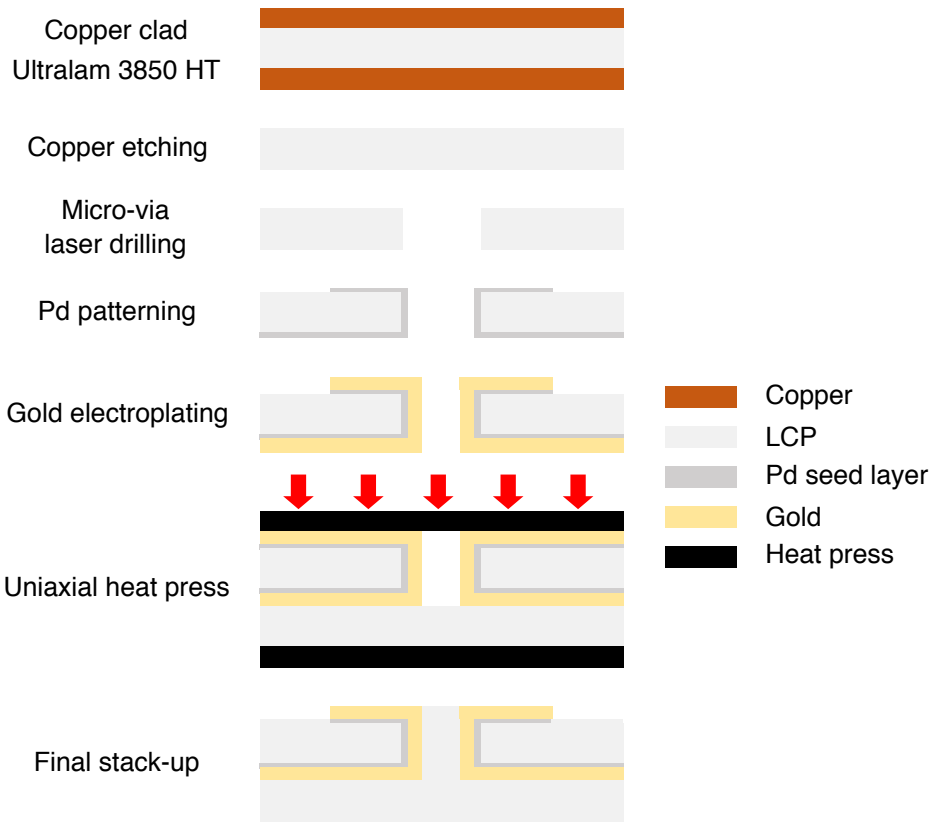

Supplemental figure 1. Copper was etched away from the Ultralam 3850 HT (Rogers Corporation) base PCB layer. Then vias were laser drilled into the LCP sheet and a Palladium (Pd) seed layer was applied to both sides of the sheet to pattern the geometry of the sensing pads (outer layer) and the interconnect traces (inner layer). Gold was then electroplated from the Pd seeds to a thickness of approximately 5 μm, to develop electrode pads and interconnect traces. The Ultralam 3908 (Rogers Corporation) encapsulation sheet was then laminated to the trace side of the array using a uniaxial press with a prescribed temperature-pressure profile over time that allowed the two LCP layers to melt and then bond during the press cycle. In this stage, LCP flowed into the micro-via gap to produce continuity of the encapsulation. Finally, the outlines of the individual arrays were laser cut from the full PCB sheet

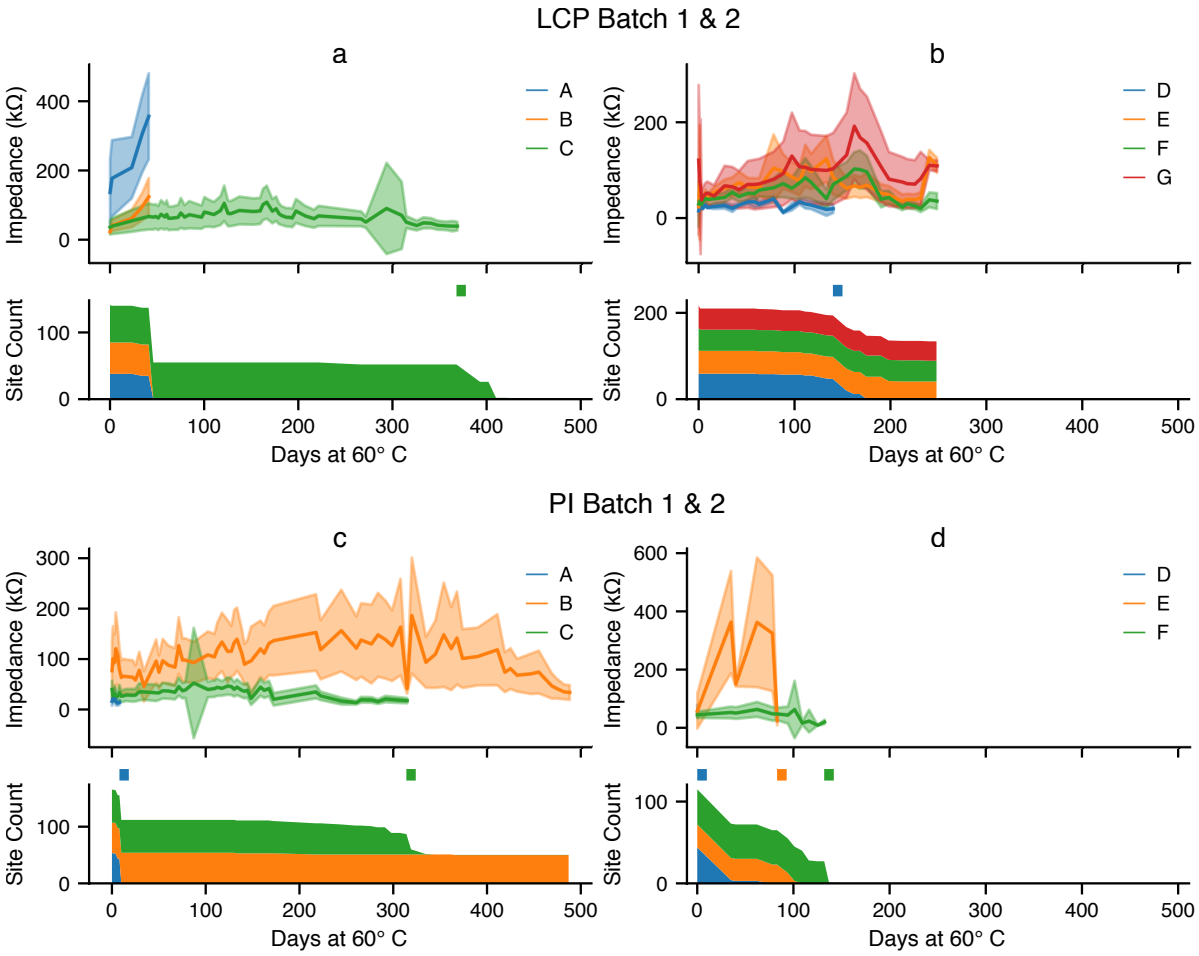

Supplemental figure 2. Accelerated aging results for LCP and PI batches. (a)-(b) Impedance and site survival series for LCP electrode batches 1 and 2. Top: 1 kHz impedance mean ± SD in shaded areas. Bottom: total surviving sites in the electrode array samples. Notches above the survival timeseries mark the observed failure point, when array yield fell below 50% of the initial number of functional sites. (Note that both detected failures in the LCP samples were determined to related to corrosion of the test chamber reference wires.) (c)-(d) Impedance and site survival series for PI electrode batches 1 & 2 (format identical to (a)-(b)). The failure of PI electrode samples were identified by delamination of the PI material.

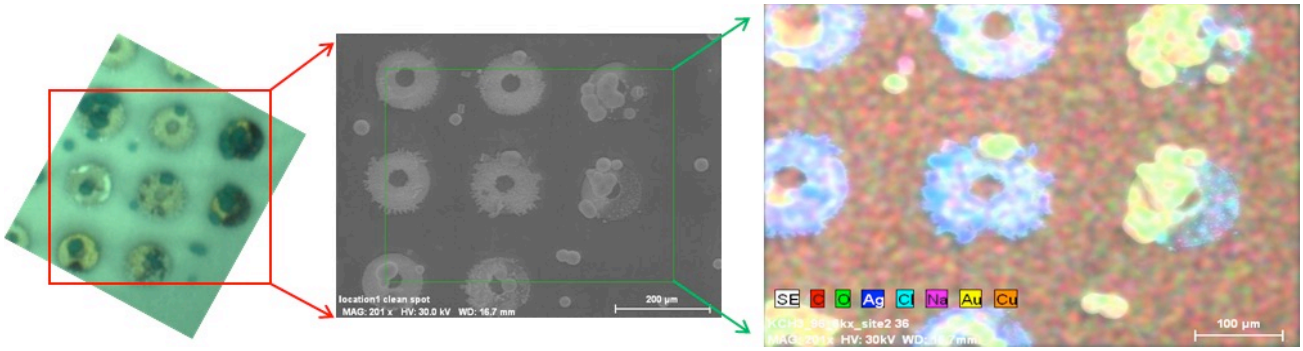

Supplemental figure 3. Surface analysis of LCP (Batch 1), Sample A after 368 days of accelerated aging. (left) Optical imaging showed both crystalline growths (silver or white in appearance) and blue-/green-colored circular clusters along the gold microcontacts. (center) SEM imaging at 200x magnification highlighted structural details; (right) Energy dispersive spectroscopy revealed: carbon (red) and oxygen (green) within the LCP encapsulation, crystals comprising silver (blue) and chloride (cyan) bonded to the metal surface, and gold (yellow) and copper (orange) deposits also along the metallic contacts. Silver, gold and copper were in solution following the corrosion of our gold-coated sterling silver reference wire; revisions for ongoing soaking studies currently employ nonpolarizable materials as a reference for long-term accelerated aging studies.

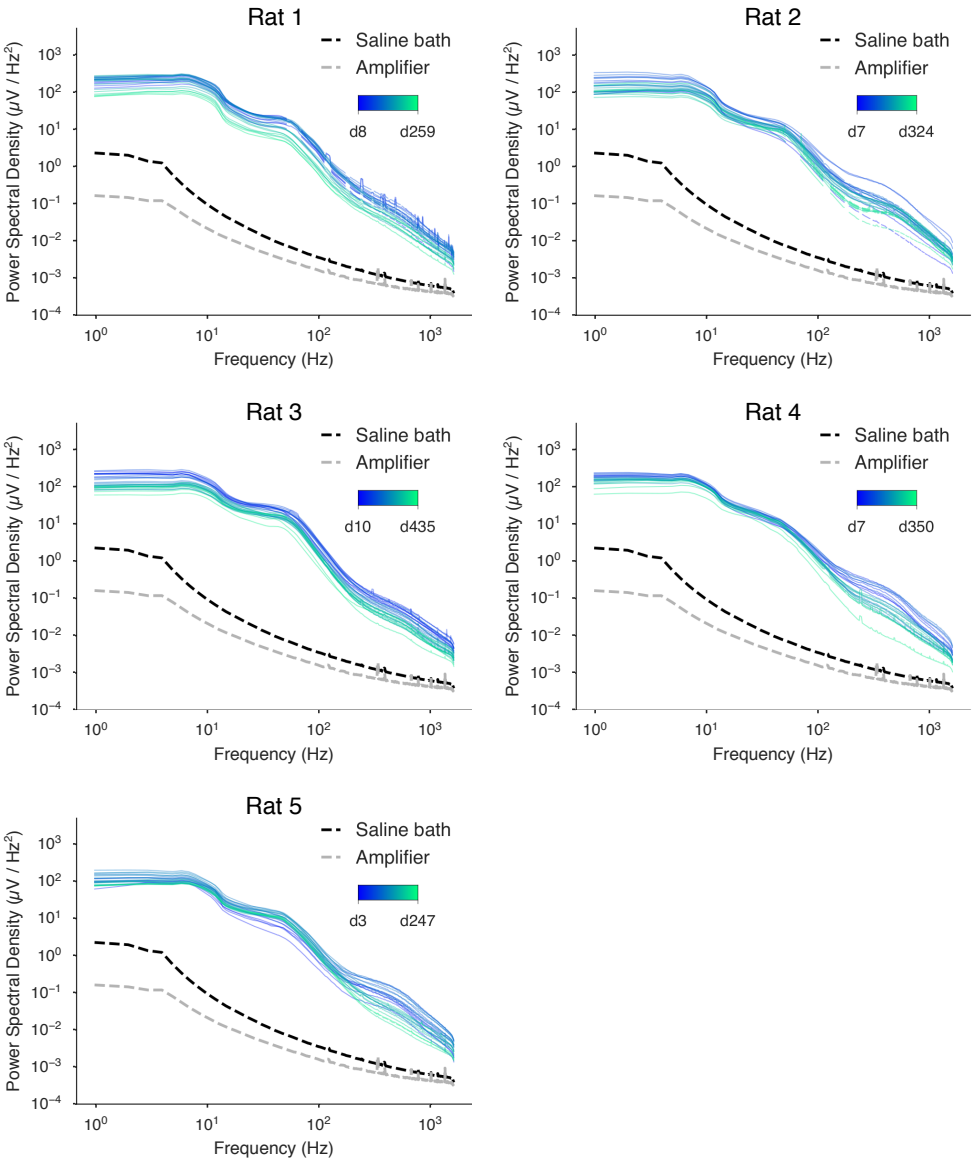

Supplemental figure 4. Power spectral density of the baseline μECoG for all awake recording sessions, shown per implant in. Reference PSDs show the background noise level of the recording system including 1) a new electrode connected to the amplifier reference through a saline bath, and 2) only the amplifier noise, with inputs shorted to ground. (The saline bath PSD was computed with a representative electrode, not an implanted electrode).

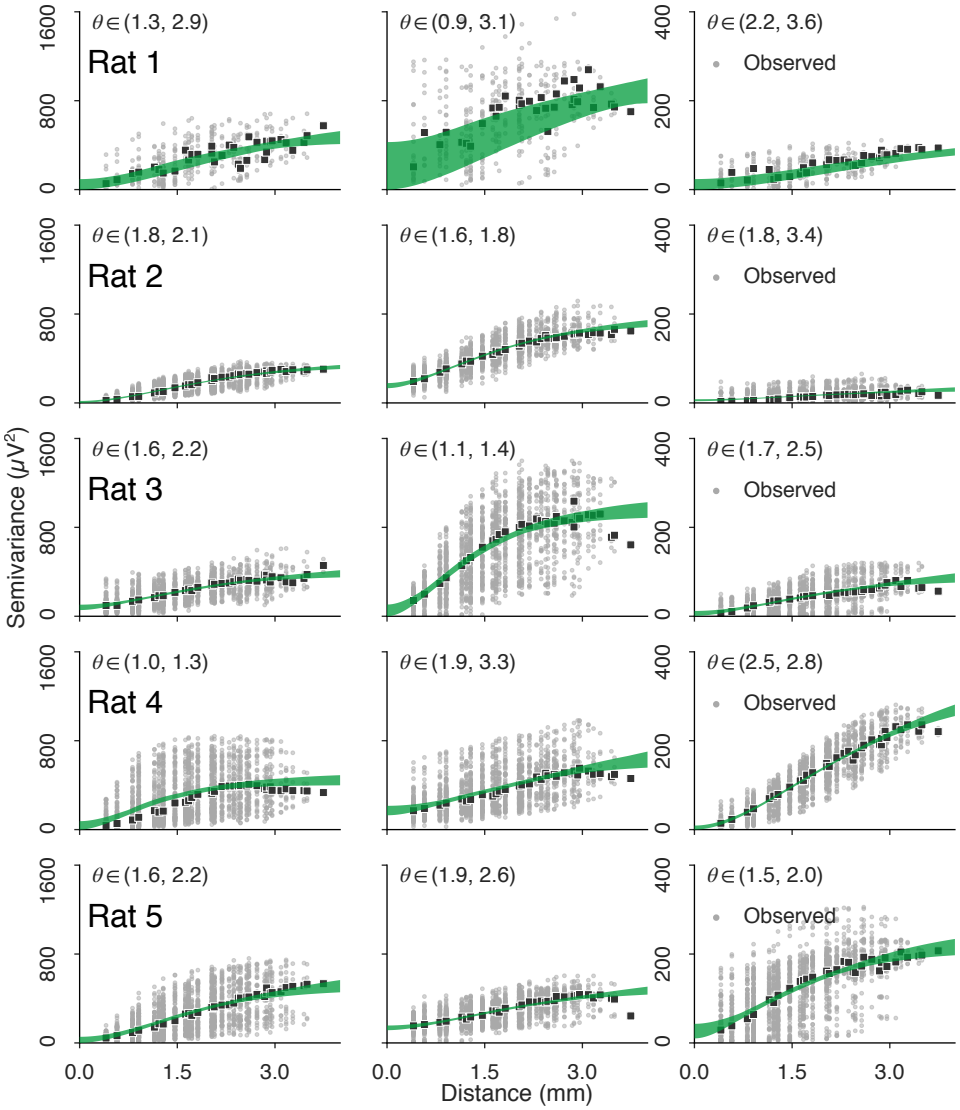

Supplemental figure 5. Observed semivariograms for select days on all implants. The full range of the estimated model posterior density is spanned by the green margin, as in figure 6(d) of the main text. The columns depict the first post-operative awake recording (left column) and a day near the peak of the signal power curves from figure 6(b) (day 70-80, middle column). The right column is a day near the end of the implant's duration (note the different ordinate scale). The parameters of the semivariance models revealed field recordings that evolved largely in amplitude (height of the curves) rather than range of correlation ($\boldsymbol{\theta}$, units of mm). In the case of Rat 1, half of the channels were mistakenly disconnected during implantation, which led to greater uncertainty in the model parameters.

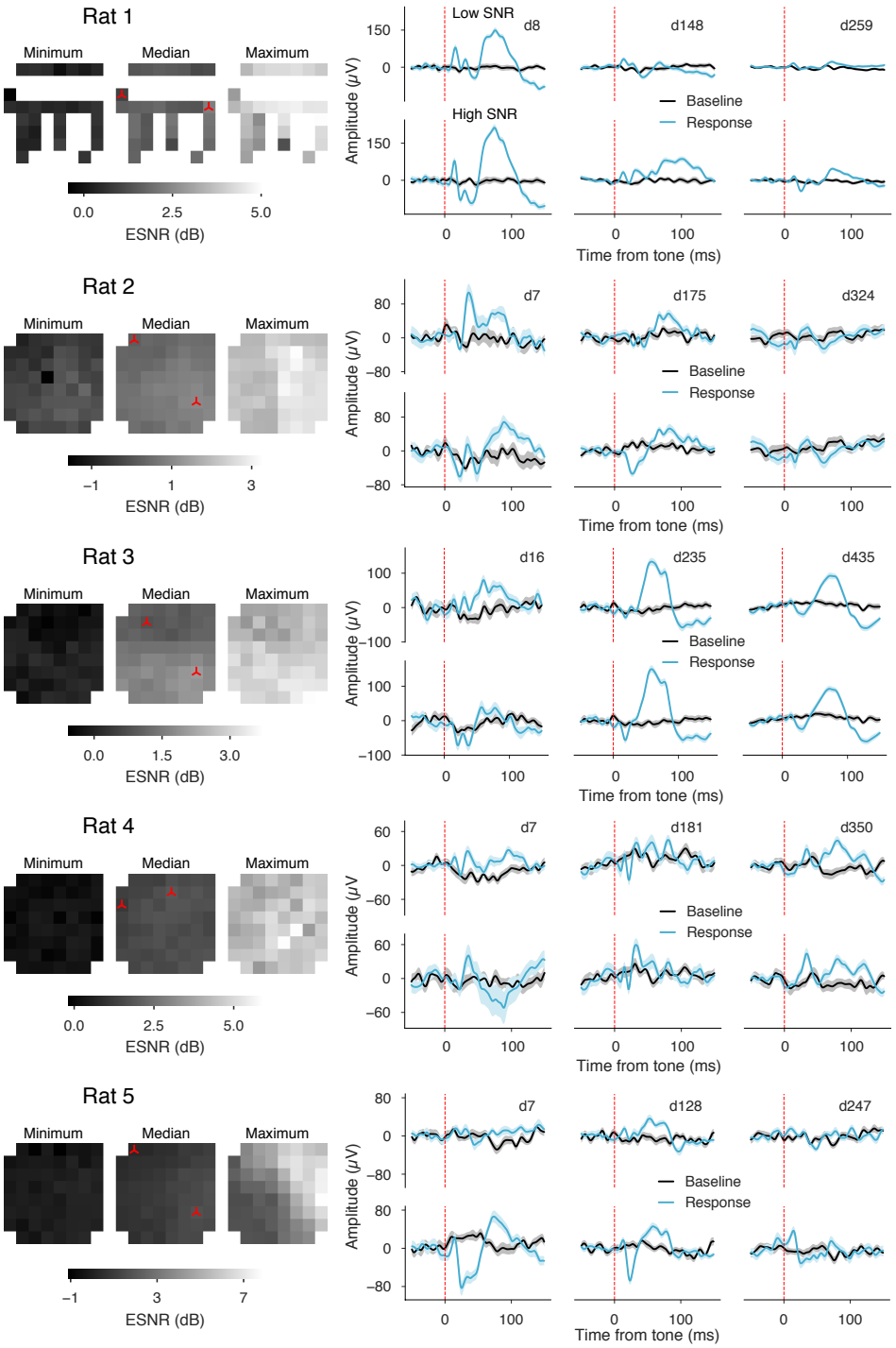

Supplemental figure 6. Longitudinal evoked responses and ESNR for all implants, after the style of figure 5 (a-b) (main text). Array-oriented heatmaps show the minimum, median, and maximum values of electrode ESNR across the duration of each implant. Response and baseline signal (trial average ± S.E.M.) for sites with low median SNR (top) and high median SNR (bottom) are displayed for early, middle, and final recording days. Half of the electrodes were not recorded from Rat 1, likely due to the electrode not being fully inserted into the ZIF connector prior to implantation, causing one row of contacts to not make connection with the ZIF connector.

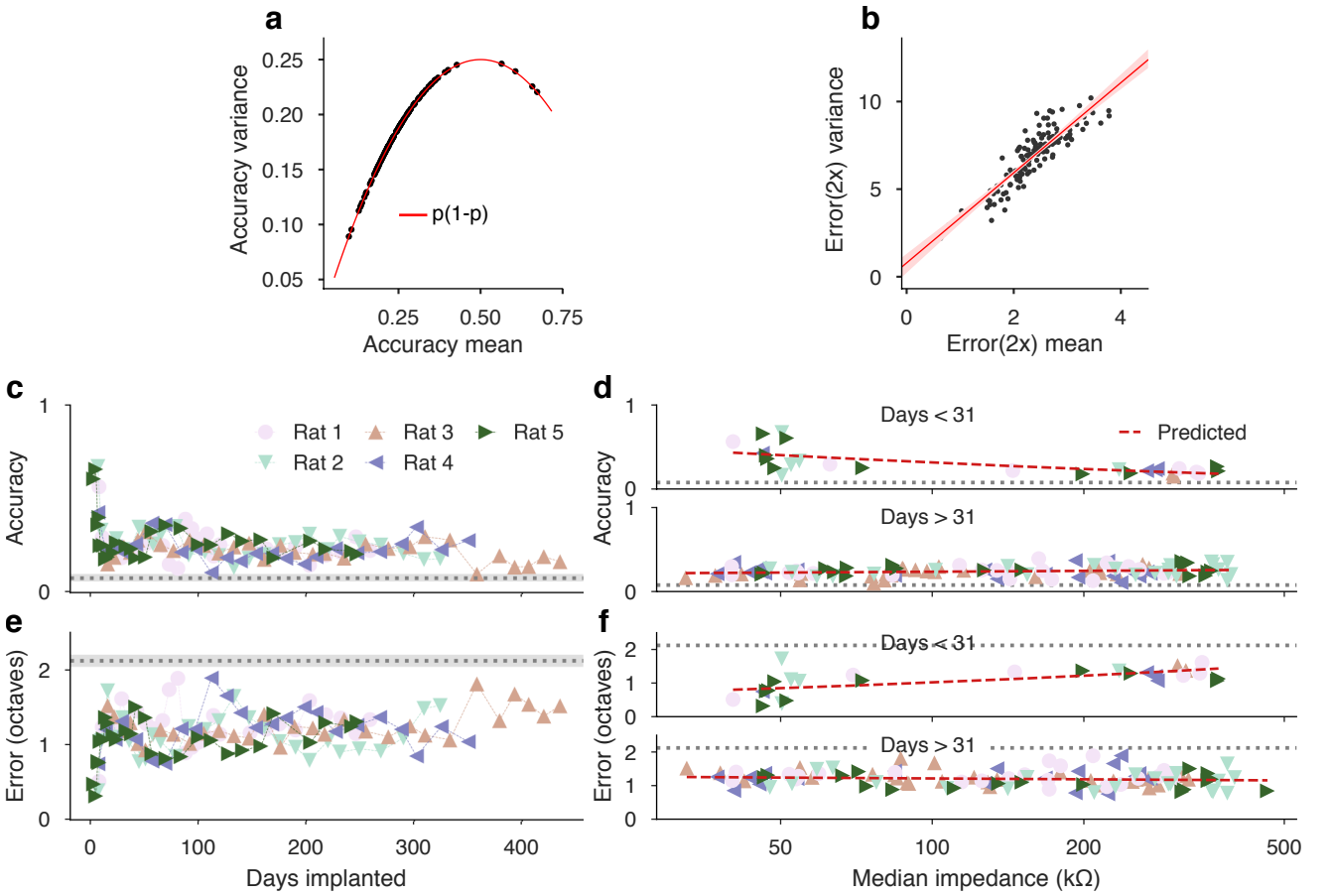

Supplemental figure 7. Generalized linear mixed regression for tone classification results. (a-b) The mean-variance relationship for each session's binary classifier accuracy reflects their binomial nature. The variance of the graded classifier error had a strong linear relationship with the graded error mean (Pearson r=0.89, $p<10^{-15}$). Graded error was converted from half-octave to integer steps to accommodate Negative Binomial regression. (c-d) Classifier accuracy decreased over the initial phase of implantation, with a significant loss of -0.385 log-odds ratio of successful prediction (from 43.3% to 18.2%) per doubling of median array impedance. In the chronic phase, while median array impedance fell, classifier accuracy also decreased with a slight but significant loss of -0.056 log-odds (25.6% to 22.0%) per halving of impedance. Impedance was fairly predictive of accuracy ($r^2_{CV} = 0.306$), although this predictive value was heavily determined in the early phase ($r^2_{CV} = 0.486$ for day < 31, and $r^2_{CV} = -0.012$ otherwise). (e-f) Classifier error increased over the initial phase with a multiplier of 1.20 per doubling of impedance, but subsequently did not vary significantly with impedance. Overall, impedance was a poor predictor of classifier error ($r^2_{CV} = 0.004$).